Available online at www.sciencedirect.com
SCIENCE DIRECT®
International Journal of Thermal Sciences 42 (2003) 343–359
International Journal of Thermal Sciences
www.elsevier.com/locate/ijts

Comparison of three discrete ordinates methods applied to two-dimensional curved geometries

Hong-Mo Koo [a], Rodolphe Vaillon [b,*], Vincent Goutière [c], Vital Le Dez [d], Hojin Cha [a], Tae-Ho Song [a]

[a] *Department of Mechanical Engineering, KAIST, 373-1, Kusong-dong, Yusong-gu, Taejon, South Korea*
[b] *Centre de thermique de Lyon, UMR CNRS 5008, INSA de Lyon, 69621 Villeurbanne cedex, France*
[c] *Groupe de recherche en ingénierie des procédés et systèmes, Université du Québec à Chicoutimi, Chicoutimi, G7H 2B1, Québec, Canada*
[d] *Laboratoire d'études thermiques, UMR CNRS 6608, ENSMA, 86961 Futuroscope cedex, France*

Received 13 January 2002; accepted 28 May 2002

Abstract

This paper describes the application and comparison of three Discrete Ordinates Methods: the Discrete Ordinates Interpolation Method (DOIM) for structured and unstructured grids; the Discrete Ordinates Method in Orthogonal Curvilinear Coordinates (DOM-OCC) for structured grid; and the Discrete Ordinates Method associated to the Finite Volume method and Ray Tracing (DOM-FV-RT) for unstructured grid. A summary of the basic equations and numerical formulations is given for each method to outline their key characteristics. In order to extract valuable information to improve DO kind methods when applied to complex geometries, they are compared in the case of radiative equilibrium of a gray medium confined between infinite black or diffusely reflecting circular or elliptical cylinders. For the circular ring problem, the three DOMs results are confronted with Monte Carlo ones for various radius ratios and radiative properties. The elliptical ring problem extends the comparison to a more complex geometry and an emphasis is put on the evaluation of wall radiation fluxes. In conclusion, distinctive features in terms of performances are observed for each method.

Keywords: Radiation; Discrete ordinates; Radiative equilibrium; Curved geometry; Structured and unstructured grids; Reflecting wall

1. Introduction

The Discrete Ordinates Method (DOM) is one of the most widespread numerical tools devoted to the solution of the Radiative Transfer Equation (RTE) in semi-transparent media. Since the first work of Chandrasekhar [1], many variations of DOM have been implemented. The common feature of all these alternatives lies in the use of a set of discrete directions, for which the intensity field is solved. With their associated weights, the resulting mathematical tool—the so-called quadrature—allows the calculation of directionally integrated radiative variables like radiative energy source terms and radiative hemispherical or net fluxes.

The variants of DOM may be classified in connection with:

- the form of the RTE to be solved: differential, integral [2], and even parity/second order [3–7],
- the kind of coordinate systems (Cartesian [8–11], cylindrical [12–16], spherical [17], and curvilinear/body fitted [5,18,19]),
- the way the spatial integration of the RTE is performed (Finite Difference, Finite Volume [20,21], Finite Element [3], direct integration along pathlengths [22,23], interpolations schemes [24–27], etc.),
- the choice of the directional quadrature set [28–33],
- the type of grid (structured and unstructured with triangles [22,23] or tetragons, parallelepipeds or tetrahedrons [34]), and then the ability for the radiation solver to be coupled with other heat transfer or energy production phenomena,

* Corresponding author.
E-mail addresses: vaillon@genserver.insa-lyon.fr (R. Vaillon), thsong@kaist.ac.kr (T.-H. Song).

1290-0729/02/$ – see front matter
doi:10.1016/S1290-0729(02)00036-4

Nomenclature

G	incident radiation	$\mathrm{W\cdot m^{-2}}$	
I	(total) radiative intensity	$\mathrm{W\cdot m^{-2}\cdot sr^{-1}}$	
I_b	(total) blackbody radiative intensity	$\mathrm{W\cdot m^{-2}\cdot sr^{-1}}$	
$\hat{\boldsymbol{n}}$	inward unit normal vector from a wall		
N_φ	number of polar angles		
N_ψ	number of azimuthal angles		
$\dot{q}$	radiative heat source per unit volume	$\mathrm{W\cdot m^{-3}}$	
q''_w	net radiative heat flux at a wall	$\mathrm{W\cdot m^{-2}}$	
W	angular quadrature weight		
r	coordinate in radial direction	m	
r^*	nondimensional distance across a cylinder		
s, n	curvilinear coordinates		
x, y	Cartesian coordinates		
T	temperature	K	

Greek symbols

β	extinction coefficient	$\mathrm{m^{-1}}$
ε	wall emissivity	
μ, ξ, η	direction cosines of a direction $\widehat{\Omega}$	
φ	polar angle	rad
κ	absorption coefficient	$\mathrm{m^{-1}}$
σ	Stefan–Boltzmann constant	$\mathrm{W\cdot m^{-2}\cdot K^{-4}}$
σ_s	scattering coefficient	$\mathrm{m^{-1}}$
τ	optical depth	
ω	scattering albedo	
ψ	azimuthal angle	rad
Φ	scattering phase function	
Φ^*	nondimensional emissive power	
Γ	inverse of a radius of curvature	$\mathrm{m^{-1}}$
$\widehat{\Omega}$	radiation propagation direction vector	
Ω	solid angle	sr
Ψ_1^*	nondimensional radiative net heat flux at outer wall	
Ψ_2^*	nondimensional radiative incident heat flux at a wall	

Indices

b	blackbody
w	related to a wall

– the skill to treat diffusely or specularly reflecting [35] boundaries, and to include scattering for any shape of phase function (isotropic and anisotropic [36,37], Lorenz–Mie [38], etc.),
– the appropriateness of the method with existing spectral radiation properties models.

The number of works about DOM is considerable, and the above reference list is not exhaustive. It should be noticed that several references should have been cited several times in the above classification, but, for the sake of simplicity, we have chosen the most representative feature of each article. Then it follows that criteria are too numerous to be able to extract an ideal method which could be applied to any kind of problem, and consume small computation time while preserving accuracy. However, by focusing on precise key characteristics, comparisons between various methods are likely to provide valuable information to improve the method.

The objective of this article is to present three different implementations of DOM and to compare them in the case of geometries with curved boundaries. A particular attention will be paid to the way radiation fluxes are calculated, and then to the precision of each procedure when reflecting walls have to be modelled.

Outlines of the methods are given in Section 2. The first procedure, the Discrete Ordinates Interpolation Method (DOIM) [6,39], is extended to cylindrical geometries. The Interpolation Method is a scheme which can be applied to unstructured grids [40] as well as structured ones. The second method is an extension of the DOM to Orthogonal Curvilinear Coordinates (DOM-OCC) [18,19], which involves a local directional frame and a conventional spatial integration scheme in structured grids. The last DOM (DOM-FV-RT), associated to the Finite Volume Method in unstructured grid, incorporates directional ray propagation relations (Ray Tracing) within the cells [22,23,34].

The test problems and results are detailed in Section 3. They have been chosen in order to focus on the treatment of geometries limited by curved walls. In particular, the ways how the incident radiation fluxes on walls are calculated are precisely compared. The first test considers the radiative equilibrium situation within infinite concentric circular cylinders with isothermal black boundaries. Results are validated against the Monte Carlo calculations of Perlmutter and Howell [41] and discussed. The problem under consideration for the second test case is the radiative equilibrium between infinite isothermal elliptical cylinders. Performances of the methods are compared and a particular attention is paid on the way incident radiation fluxes on walls are calculated.

2. Formulations of methods

2.1. Discrete ordinates interpolation method (DOIM)

2.1.1. Mathematical formulation

The detailed formulation of the Discrete Ordinates Interpolation Method can be found in the reference [6,39]. Here is given only a summary of the DOIM.

In the DOIM, the Radiative Transfer Equation (RTE) is replaced by a set of equations for a finite number of ordinate directions $\widehat{\Omega}_i$, $i = 1, 2, \ldots, M$, and the scattering

term integral is replaced by a quadrature of order M with appropriate angular weights W_i as:

$$\frac{1}{\beta}\frac{\mathrm{d}I_i}{\mathrm{d}s_i} = -I_i + \dot{S}_i \tag{1}$$

where:

$$\dot{S}_i = (1-\omega)I_b + \frac{\omega}{4\pi}\sum_{k=1}^{M} I_k \Phi\big(\widehat{\Omega}_k, \widehat{\Omega}_i\big) W_k \tag{2}$$

and where I_i is the intensity at a position $\hat{\mathbf{r}}$ for a direction $\widehat{\Omega}_i$; $\beta(=\kappa+\sigma_s)$ is the extinction coefficient; κ and σ_s are the absorption and the scattering coefficients; ω is the scattering albedo; and $\Phi(\widehat{\Omega}_k, \widehat{\Omega}_i)$ is the scattering phase function of intensity entering from $\widehat{\Omega}_k$ and leaving to $\widehat{\Omega}_i$. The boundary condition at a diffuse wall is given by:

$$I_i = \varepsilon I_{bw} + \frac{1-\varepsilon}{\pi}\sum_{\hat{\boldsymbol{n}}\cdot\widehat{\Omega}_k<0} \big|\hat{\boldsymbol{n}}\cdot\widehat{\Omega}_k\big| I_k W_k, \quad \hat{\boldsymbol{n}}\cdot\widehat{\Omega}_i > 0 \tag{3}$$

where ε is the wall emissivity, I_{bw} is the blackbody intensity of the wall, and $\hat{\boldsymbol{n}}$ is the inward unit normal vector from the wall. Eq. (1), together with the boundary condition (3), constitutes a set of M simultaneous, first order, linear differential equations.

The local medium temperature may be obtained, when it is not known, from the pointwise energy balance equation iteratively as:

$$\sum_{k=1}^{M} \kappa I_k W_k - 4\pi\kappa I_b + \dot{q} = 0 \tag{4}$$

where $\dot{q}$ is the radiative strength of the heat source per volume unit. Also, the net radiative heat flux at a wall with normal vector $\hat{\boldsymbol{n}}$ can be found by:

$$q''_w = \sum_{k=1}^{M} \big(\hat{\boldsymbol{n}}\cdot\widehat{\Omega}_k\big) I_k W_k \tag{5}$$

2.1.2. Angular quadrature scheme

The ordinate $\widehat{\Omega}_i$ and angular weight W_i can be arbitrarily obtained [42]. Among them, the Piecewise Constant Angular (PCA) quadrature is employed in this study. Briggs et al. [43] showed that this approximation could mitigate the ray effects of the standard S_N quadrature for the even-parity equations.

In the PCA quadrature, the total solid angle is divided uniformly in the polar (φ) and azimuthal (ψ) directions (see Fig. 1). The numbers of divisions are denoted by N_φ and N_ψ, and the specific PCA quadrature is denoted by $N_\varphi \times N_\psi$. From this we can express discrete polar and azimuthal angles as follows:

$$\begin{aligned} &\varphi_n = (n-1/2)\cdot\Delta\varphi, \quad n = 1,2,\ldots,N_\varphi (0 \leqslant \varphi \leqslant \pi) \\ &\psi_m = (m-1)\cdot\Delta\psi, \quad m = 1,2,\ldots,N_\psi (0 \leqslant \psi \leqslant 2\pi) \end{aligned} \tag{6}$$

where $\Delta\psi = 2\pi/N_\psi$ and $\Delta\varphi = \pi/N_\varphi$. For each discrete ordinate, the corresponding weight is obtained as:

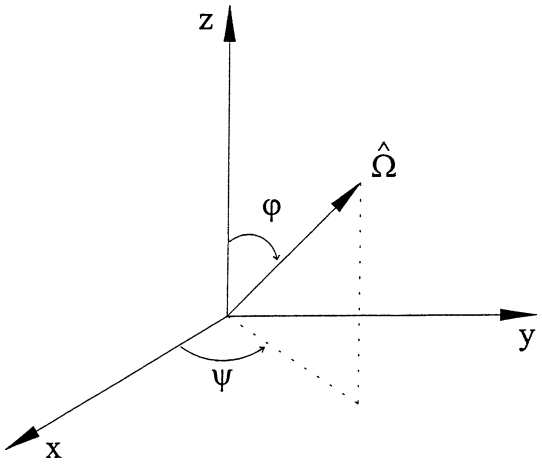

Fig. 1. A typical ordinate direction of the DOIM.

$$\begin{aligned} W_{mn} &= \int_{\psi_{m-1/2}}^{\psi_{m+1/2}} \int_{\varphi_{n-1/2}}^{\varphi_{n+1/2}} \sin\varphi_n \,\mathrm{d}\varphi\,\mathrm{d}\psi \\ &= (\psi_{m+1/2} - \psi_{m-1/2})(\cos\varphi_{n-1/2} - \cos\varphi_{n+1/2}) \end{aligned} \tag{7}$$

where:

$$\varphi_{j+1/2} = (\varphi_j + \varphi_{j+1})/2 \tag{8a}$$

$$\psi_{i+1/2} = (\psi_i + \psi_{i+1})/2 \tag{8b}$$

At boundary nodes, there can be solid angle overlaps [44], and simple approximation is used for the DOIM here. That is to say, if the mean direction of an overlapped solid angle is outgoing, all the rays in the solid angles is considered to be outgoing, and vice versa.

2.1.3. Discretization equation for the DOIM with interpolation scheme

The DOIM is characterized by the employment of solution of the RTE along a line of sight from upstream node to the nearest node instead of taking an arbitrary relation between nodal intensities and control volume face intensities, i.e., spatial differencing scheme used in the DOM. In this study both structured and unstructured (with triangular cells) grid systems are used for DOIM.

Consider a line of sight in direction $\widehat{\Omega}$ passing through a nodal-point P as shown in Fig. 2 (for simplicity, subscript i for the ordinate is omitted hereafter). Eq. (1) is rewritten as:

$$\frac{\mathrm{d}I}{\mathrm{d}s} + \beta I = \beta\dot{S} \tag{9}$$

The source term $\dot{S}$ is approximated by the first two terms of a Taylor series expansion about point P as follows:

$$\dot{S} = \dot{S}(s) = \dot{S}_P + \left.\frac{\mathrm{d}\dot{S}}{\mathrm{d}s}\right|_P (s - \Delta s) \tag{10}$$

Given the boundary values I_{IN}, Eq. (9) can be exactly solved for I_P for constant β, i.e.:

$$I_P = I_{IN}e^{-\beta\Delta s} + \dot{S}_P\left(1-e^{-\beta\Delta s}\right) - \frac{1}{\beta}\frac{\mathrm{d}\dot{S}}{\mathrm{d}s}\bigg|_P\left[1-e^{-\beta\Delta s}(1+\beta\Delta s)\right] \quad (11)$$

where I_{IN} is a non-grid value interpolated with its neighboring values of I by a linear polynomial [6,40], which is expressed as follows:

$$I_{IN} = \begin{cases} \sum_{n=0}^{1} L_n I(l-1+n, m-1) \\ \quad \text{for structured grid system} \\ \sum_{n=0}^{1} L_n I_{n+1} \\ \quad \text{for unstructured grid system} \end{cases} \quad (12)$$

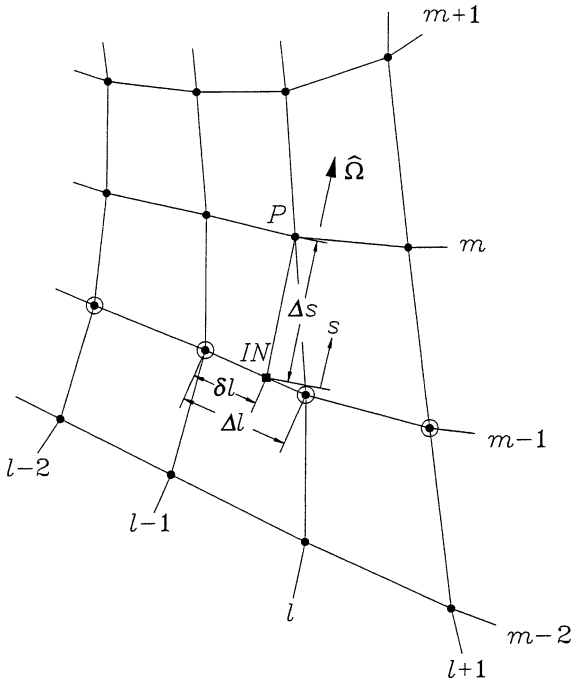

(a)

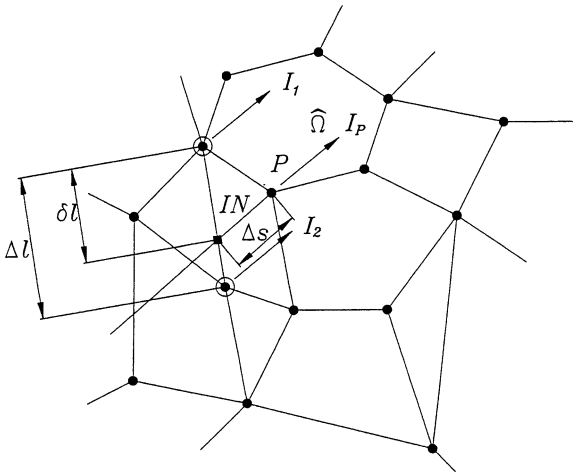

(b)

Fig. 2. Grid notation for discretization equation of the DOIM (a) structured grid and (b) unstructured grid.

where l and m are grid indices in the figure, $L_0 = \frac{\Delta l-\delta l}{\Delta l}$ and $L_1 = \frac{\delta l}{\Delta l}$. The gradient $\dot{S}$ in Eq. (10) can be obtained from the following discretization equation:

$$\frac{\mathrm{d}\dot{S}}{\mathrm{d}s}\bigg|_P = \frac{\dot{S}_P - \dot{S}_{IN}}{\Delta s} \quad (13)$$

where $\dot{S}_{IN}$ is interpolated in the same way as I_{IN}.

Discretization equation for I_P in terms of its neighboring values of I and $\dot{S}$ is obtained when Eqs. (12) and (13) are introduced to Eq. (11), but the resulting equation is not given here owing to the limited space.

2.2. Discrete ordinates method in orthogonal curvilinear coordinates (DOM-OCC)

An extension of the discrete ordinates method in orthogonal curvilinear coordinates has been performed by Vaillon et al. for (s, n, z) [18] and (s, n, θ) [19] coordinates systems. A detailed description of the technique is available in these references. We present here a summary of the main features of the mathematical and numerical formulations, as well as some improvements of the method.

2.2.1. Mathematical formulation

The radiation intensity $I(P, \widehat{\Omega})$ at a point P along a direction $\widehat{\Omega}$ depends on the three position coordinates of the point P and two polar angles which define the direction of propagation in space. Commonly, the same system of coordinates is used to specify both the position and the direction of propagation under consideration. This is the case for DOIM (Section 2.1) and for DOM-FV-RT (Section 2.3). As for DOM-OCC, the geometry is defined in a fixed spatial orthogonal curvilinear coordinates system, whereas a local moving directional frame is employed (Fig. 3) to specify the direction of ray propagation.

As a consequence, the expression of the pathlength derivative of radiation intensity in the conservative form of the RTE contains additional angular redistribution terms, accounting for variations of the polar angles (φ, ψ) with the position coordinates (x_1, x_2, x_3), when the direction under

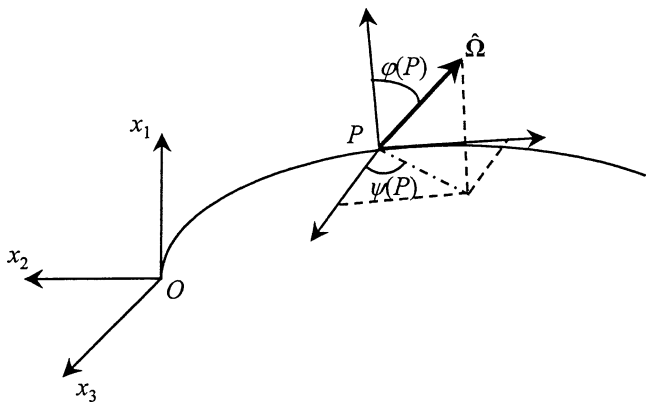

Fig. 3. Fixed spatial coordinates system and local (P) directional frame for the DOM-OCC.

consideration is fixed in the local directional coordinates system. As an example, in the case of a two-dimensional geometry described in orthogonal (*s,n*) spatial coordinates, the corresponding RTE can be expressed as:

$$\frac{\sin\varphi\sin\psi}{1+\Gamma n}\frac{\partial I}{\partial s}+\frac{\cos\varphi}{1+\Gamma n}\frac{\partial(1+\Gamma n)I}{\partial n}+\frac{\Gamma}{1+\Gamma n}\left[\frac{\sin^2\psi}{\sin\varphi}\frac{\partial\sin^2\varphi I}{\partial\varphi}+\cos\varphi\frac{\partial\sin\psi\cos\psi I}{\partial\psi}\right]=\kappa(I_b-I) \tag{14}$$

where Γ is the inverse of the radius of curvature of the line on which the curvilinear coordinate (s) is defined.

Further details about the development of the RTE in various orthogonal curvilinear coordinates systems can be found in Refs. [18,19].

2.2.2. Discretized form of the RTE: Finite volume method and discrete ordinates

The medium described in the orthogonal curvilinear coordinates system is discretized in a structured grid system. The angular space is also discretized into discrete solid angles $\Delta\Omega_{nm}$ associated to discrete directions (φ_n, ψ_m). A Finite Volume procedure is employed and it consists of integrating the RTE over each cell ($\Delta V_{ijk} = \Delta x_1 \Delta x_2 \Delta x_3$) and over each finite solid angle ($\Delta\Omega_{nm}$). Angular integrals are replaced by numerical quadratures which express angular variables as functions of their values at the selected discrete directions.

The treatment of angular redistribution terms and the resulting discretized form of the RTE are not reported here and can be found in Refs. [18,19].

2.2.3. Boundary conditions: Reflecting walls and symmetry

Thanks to the use of a local directional coordinates system, the calculation of radiation fluxes incident on walls and the handling of axis or plane symmetry conditions can be performed without any difficulty. Since tangent planes of walls always coincide with a coordinates plane of the local directional frame, there is no control solid angle overhang at boundaries and the selection of discrete ordinates for the reckoning of incident fluxes is obvious. All the same, plane or axis symmetry conditions can be treated easily because this plane (or axis) of symmetry generally corresponds to a plane of coordinates (or to one of the axes) of the body fitted coordinates system and the set of discrete directions is chosen so that it respects the same symmetry condition. This particular feature can be used to reduce the spatial domain for the computation of solutions when symmetry conditions may be extracted from the geometrical and physical configuration under consideration.

2.2.4. Numerical scheme

As in classical formulations of original Discrete Ordinates Methods [12], the unknown intensities appearing in the discretized form of the RTE (values on cells and solid angles faces) are eliminated by using conventional interpolation schemes. Our previous experience on the present method demonstrated that a step scheme is recommended for spatial differencing to ensure positive intensities whereas a diamond scheme is convenient for differencing the directional terms regardless of any stability consideration. Thanks to the use of a local directional coordinate system, the scanning of medium is easily performed from cell to cell, provided that the beginning mesh is properly selected.

The choice of a set of discrete directions and of the associated weights for the calculation of angular integrated values is crucial, particularly when reflecting wall boundary conditions are encountered. The objective is to reduce the number of directions while preserving accuracy. For the DOM-OCC, the angular dependence is expressed as functions of the polar and azimuthal angles. As a consequence, among the existing quadratures, our choice is restricted to polar and azimuthal discretizations; N_φ discrete polar angles and N_ψ discrete azimuthal angles associated to $N_\varphi \times N_\psi$ non-overlapped discrete solid angles. In this work, the discretization is uniform in the azimuthal direction. As for polar angles, our experience in DOM showed that a uniform division in cosine of the polar angle produces better results than a uniform polar angle discretization. Finally, the selection of weights can be performed separately for the calculation of incident radiation values G and net radiative heat flux at a wall with normal vector $\hat{\boldsymbol{n}}$:

$$G=\int_{4\pi} I\left(\widehat{\Omega}\right)\mathrm{d}\Omega=\sum_{n=1}^{N_\varphi}\sum_{m=1}^{N_\psi} W_{G,nm}\, I(\varphi_n,\psi_m) \tag{15}$$

$$q''_w=\int_{4\pi}\left(\hat{\boldsymbol{n}}\cdot\widehat{\Omega}\right)I\left(\hat{\Omega}\right)\mathrm{d}\Omega=\sum_{n=1}^{N_\varphi}\sum_{m=1}^{N_\psi} W_{q'',nm}\, I(\varphi_n,\psi_m) \tag{16}$$

where $W_{G,nm}$ and $W_{q''_w,nm}$ are the weights used for evaluation of G and q''_w, respectively.

For this work, we use a Piecewise Constant Angular (PCA) approximation slightly modified by considering a uniform polar angle cosine discretization ($\Delta\mu = \Delta(\cos\varphi)$) instead of a uniform polar angle division ($\Delta\varphi$). Then the polar angle associated to each $\Delta\mu$ interval is the inverse cosine of the mean μ value of the $\Delta\mu$ interval. To calculate any integral of angular functions, we use the equal weights rule:

$$\int_{4\pi} F\left(\widehat{\Omega}\right)\mathrm{d}\Omega=\sum_{n=1}^{N_\varphi}\sum_{m=1}^{N_\psi} W\, F(\varphi_n,\psi_m) \tag{17}$$

where W is simply given by $4\pi/(N_\varphi N_\psi)$.

As a consequence, the weights employed to calculate the incident radiation ($F = I$) is given by:

$$W_{G,nm}=cst.=W=\frac{4\pi}{N_\varphi N_\psi} \tag{18}$$

and the weights $W_{q''_w,nm}$, when net radiation fluxes along the polar direction $\hat{\boldsymbol{n}}$ are sought ($F = \cos\varphi I$), are:

$$W_{q''_w,nm} = W\cos\varphi_n = \frac{4\pi}{N_\varphi N_\psi}\cos\varphi_n \tag{19}$$

Although moments rules do not give any absolute insurance of accuracy, it may be noted as an indication that both approaches verify zero order moment, first order total and half moments rules.

2.3. Discrete ordinates method associated to the finite volume method and ray tracing (DOM-FV-RT)

2.3.1. Finite volume method

A first step consists in the generation of an unstructured grid of triangular (in the two-dimensional case) or tetrahedral (in the three-dimensional case) meshes covering the system to be studied. The radiative transfer equation is then integrated on a mesh, and leads to, applying the Gauss's theorem, in the two-dimensional case (for the three-dimensional case, see [34]):

$$\begin{aligned}&\frac{1}{\beta S^i}\sum_{k=1}^{3}\left(\hat{\Omega}\cdot\hat{\boldsymbol{n}}_k^i\right)l_k^i I_k^i\left(\widehat{\Omega}\right) + I^i\left(\widehat{\Omega}\right)\\ &\quad = (1-\omega)I_b^i + \frac{\omega}{4\pi}\int\limits_{\Omega'=4\pi}\Phi\left(\widehat{\Omega}'\to\widehat{\Omega}\right)I^i\left(\widehat{\Omega}'\right)\mathrm{d}\Omega'\end{aligned} \tag{20}$$

where $\hat{\boldsymbol{n}}_k^i$ is the external unit normal vector on length k of the mesh i, and the mean integrated surface and line intensities are defined as:

$$\begin{aligned}&I^i\left(\widehat{\Omega}\right) = \frac{1}{S^i}\int\limits_{S^i} I\left(s,\widehat{\Omega}\right)\mathrm{d}S \quad \text{and}\\ &I_k^i\left(\widehat{\Omega}\right) = \frac{1}{l_k^i}\int\limits_{l_k^i} I\left(s,\widehat{\Omega}\right)\mathrm{d}l\end{aligned} \tag{21}$$

The integral term due to scattering in the RTE is approximated by a discrete sum, leading to:

$$\begin{aligned}&I_m^i - \frac{\omega}{4\pi}\sum_{m'=1}^{M} W_{m'}\Phi_{m'm}I_{m'}^i\\ &\quad = (1-\omega)I_b^i - \frac{1}{\beta S^i}\sum_{k=1}^{3}\zeta_{km}^i l_k^i I_{km}^i\end{aligned} \tag{22}$$

where M is the number of propagation directions, $\zeta_{km}^i = \widehat{\Omega}_m\cdot\hat{\boldsymbol{n}}_k^i$ and $W_{m'}$ is the weight associated to the discrete direction $\widehat{\Omega}_{m'}$. The discrete diffuse reflection boundary conditions on the physical surfaces of the system are:

$$\begin{aligned}&I^{\mathrm{out}}\left(\widehat{\Omega}_m\right) = \varepsilon I_{bw} + \frac{1-\varepsilon}{\pi}\sum_{\left(\hat{\boldsymbol{n}}\cdot\widehat{\Omega}_{m'}\right)>0} W_{m'}\left(\hat{\boldsymbol{n}}\cdot\widehat{\Omega}_{m'}\right)I^{\mathrm{in}}\left(\widehat{\Omega}_{m'}\right)\\ &\quad\text{for } \left(\hat{\boldsymbol{n}}\cdot\widehat{\Omega}_m\right) < 0\end{aligned} \tag{23}$$

where $I^{\mathrm{out}}(\widehat{\Omega}_m)$ is the intensity leaving the boundary surface for the discrete direction $\widehat{\Omega}_m$, $I^{\mathrm{in}}(\widehat{\Omega}_{m'})$ is the incoming intensity on the boundary surface for the discrete direction $\widehat{\Omega}_{m'}$, $\hat{\boldsymbol{n}}$ is the unit external normal vector of the boundary surface, ε is the emissivity of the wall and I_{bw} is the blackbody intensity of the wall.

The linear system to be solved to obtain the mean surface intensities is not closed because of the unknown line intensities on the boundaries of the cells: in the standard discrete ordinates method, the line intensities are interpolated to close the previous system. Such a procedure is acceptable in structured square or rectangular meshes, but for triangular unstructured cells this is inappropriate. To avoid interpolations in triangular cells, a ray tracing algorithm is used for each discrete direction of propagation.

2.3.2. Ray tracing in triangular cells

The formal solution of the RTE along a bounded path defined by its direction $\widehat{\Omega}$ is:

$$\begin{aligned}&I\left(s_f,\widehat{\Omega}\right)\\ &\quad = I\left(s_i,\widehat{\Omega}\right)e^{-\beta t} + \beta\int\limits_{s=s_i}^{s_f}\left[(1-\omega)I_b(s)\right.\\ &\qquad\left.+\frac{\omega}{4\pi}\int\limits_{\Omega'=4\pi}\Phi\left(\widehat{\Omega}'\to\widehat{\Omega}\right)I\left(s,\widehat{\Omega}'\right)\mathrm{d}\Omega'\right]\\ &\qquad\times e^{-\beta(s_f-s)}\,\mathrm{d}s\end{aligned} \tag{24}$$

where s_i is the beginning of the path, s_f is the end of the path and $t = s_f - s_i$ is the path length. If one supposes the intensity and the Planck function constant in a mesh, the previous equation leads to:

$$\forall m\in\{1,\ldots,M\}\quad I_m^{s_f} = I_m^{s_i}e^{-\beta t} + J_m^i\left(1-e^{-\beta t}\right) \tag{25}$$

with:

$$J_m^i = (1-\omega)I_b^i + \frac{\omega}{4\pi}\sum_{m'=1}^{M} W_{m'}\Phi_{m'm}I_{m'}^i \tag{26}$$

in the previous equation, $I_m^{s_f}$ is the intensity on a length of a mesh i from the intensity $I_m^{s_i}$ on an other side of this mesh. For instance, the mean intensity on side 1 of a triangular mesh is (Fig. 4):

$$I_{1m}^i = \frac{1}{l_1^i}\int\limits_{p_1=0}^{l_1^i} I_{1m}(p_1)\,\mathrm{d}p_1 \tag{27}$$

The evaluation of the integral easily leads to [22,23]:

$$\begin{aligned}I_{1m}^i \;=\; & I_{2m}^i\frac{\sin\alpha_1\sin\gamma_2}{\sin\alpha_3\sin\gamma_1}\frac{1-e^{-\tau}}{\tau}\\ &+ I_{3m}^i\frac{\sin\alpha_2\sin\gamma_3}{\sin\alpha_3\sin\gamma_1}\frac{1-e^{-\tau}}{\tau}\\ &+ J_m^i\left(1-\frac{1-e^{-\tau}}{\tau}\right)\end{aligned} \tag{28}$$

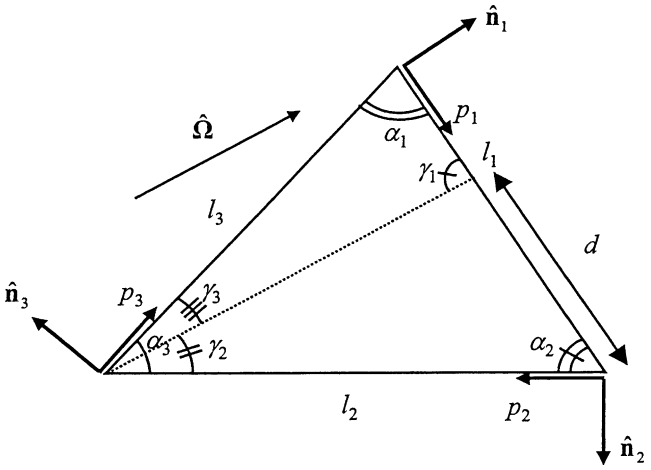

Fig. 4. A triangular cell and the associated angular sectors defined for the DOM-FV-RT.

where:

$$\tau = \frac{\beta l_2^i}{\sqrt{\mu^2+\xi^2}} \frac{\sin\alpha_2}{\sin\gamma_1} = \frac{\beta l_3^i}{\sqrt{\mu^2+\xi^2}} \frac{\sin\alpha_1}{\sin\gamma_1} \tag{29}$$

(μ, ξ, η) being the direction cosines of the propagation direction $\widehat{\Omega}$.

To cover the whole directional quadrature, one must add five other angular sectors in the triangular mesh and establish analogous equations to the previous one.

3. Application results and discussion

The three variations of the DOM are now applied to two-dimensional problems. In order to carefully analyze the results of the three DOMs, an absorbing, emitting and nonscattering medium is considered. Two problems are examined in this study. The first one deals with an infinite circular ring and the other one, with an infinite elliptical ring. Both enclosures have diffuse and isothermal walls and in both problems, the medium is assumed to be at radiative equilibrium. In the remaining sections, all the computational results for each method were taken when the solution accuracy hardly varied with increasing the number of spatial and angular ordinates.

3.1. Circular ring problem

The schematic is shown in Fig. 5(a). The emissivities of the inner and outer walls are varied as 0.1, 0.3 and 1. The optical depth $\tau(\equiv \kappa(r_1 - r_2))$ is varied as 0.1, 2 and 10. The radius ratio (r_2/r_1) is varied as 0.01, 0.1 and 0.5. The nondimensional distance across the cylinders (r^*), emissive power (Φ^*) and heat flux at outer wall (Φ_1^*) are defined as follows:

$$r^* = (r - r_2)/(r_1 - r_2) \tag{30}$$

$$\Phi^*(r) = \frac{T^4(r) - T_1^4}{T_2^4 - T_1^4} \tag{31}$$

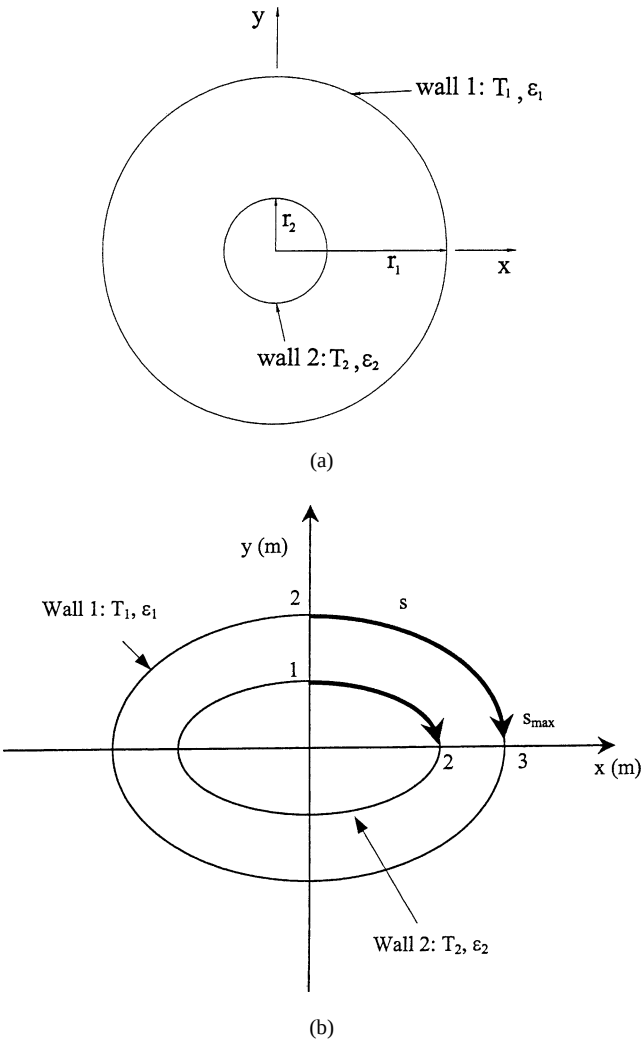

Fig. 5. Schematics of the two-dimensional (a) circular ring and (b) elliptical ring.

$$\Psi_1^* = \frac{r_1}{r_2} \frac{q_w''(r_1)}{\sigma(T_2^4 - T_1^4)} \tag{32}$$

Before presenting application results of the three DOMs, the numbers of spatial grids (or triangular cells for the DOIM (unstructured) and DOM-FV-RT) and angular ordinates used for each of them are mentioned first. They are given in Table 1. Since the DOIM and the DOM-FV-RT use Cartesian coordinates and angular ordinates fixed in space, they cannot use circumferential symmetry and they have to consider the entire domain for their calculation. As the DOM-OCC uses a local directional coordinate system and an azimuthal symmetry exists in this problem, some simplifications of the domain can be made with this method: the problem is essentially one-dimensional in radial direction and the DOM-OCC calculates only a quarter of the entire circular ring. As a result, the DOM-OCC considers a really smaller number of angular ordinates than the two other DOMs. The DOM which generally employs the largest number of angular ordinates is the DOM-FV-RT; it uses a T_5 angular quadrature.

Table 1
Numbers of spatial grids (or triangular cells) and angular ordinates taken for the entire circular ring

Test cases	DOM-OCC*		DOM-FV-RT		DOIM (structured)		DOIM (unstructured)	
	No. of spatial grids	No. of angular ordinates	No. of triangular cells	No. of angular ordinates	No. of spatial grids	No. of angular ordinates	No. of triangular cells	No. of angular ordinates
$\varepsilon_1=\varepsilon_2=1$, $\tau=2, r_2/r_1=0.5$	1120	6	5000	100	7200	120	5128	120
$\varepsilon_1=\varepsilon_2=1$, $\tau=2, r_2/r_1=0.1$	1680	8	5000	100	3600	60	5280	60
$\varepsilon_1=\varepsilon_2=1$, $\tau=2, r_2/r_1=0.01$	5600	8	5000	100	14400	60	5230	60
$\varepsilon_1=\varepsilon_2=1$, $\tau=10, r_2/r_1=0.1$	1680	6	5000	100	7200	60	5280	60
$\varepsilon_1=\varepsilon_2=1$, $\tau=0.1, r_2/r_1=0.1$	1680	10	5000	100	7200	60	5280	60
$\varepsilon_1=\varepsilon_2=0.3$, $\tau=2, r_2/r_1=0.1$	5600	8	5000	100	900	60	5280	60
$\varepsilon_1=\varepsilon_2=0.1$, $\tau=2, r_2/r_1=0.1$	5600	8	5000	100	900	60	5280	240

* For the DOM-OCC, actual number of spatial grids taken in the calculation is a quarter of the value given in this table.

Table 2
Nondimensional outer wall heat fluxes by Monte Carlo and the three DOMs, and the three DOMs relative discrepancies with respect to Monte Carlo results in the circular ring problem

Test cases	Monte Carlo method	DOM OCC (standard deviation)	RD* of DOM-OCC(%)	DOM-FV-RT (standard deviation)	RD* of DOM-FV-RT(%)	DOIM-structured (standard deviation)	RD* of DOIM-structured (%)	DOIM-unstructured (standard deviation)	RD* of DOIM-unstructured (%)
$\varepsilon_1=\varepsilon_2=1$, $\tau=0.1, r_2/r_1=0.1$	0.98	1.07 (0)	9.18	0.985 (0.033)	0.51	1.14 (3.02E−3)	16.33	1.06 (4.38E−2)	0.82
$\varepsilon_1=\varepsilon_2=1$, $\tau=2, r_2/r_1=0.1$	0.784	0.872 (0)	11.22	0.794 (0.006)	1.28	0.808 (2.19E−4)	3.06	0.810 (8.06E−3)	3.32
$\varepsilon_1=\varepsilon_2=1$, $\tau=10, r_2/r_1=0.1$	0.382	0.442 (0)	15.71	0.387 (0.013)	1.31	0.347 (2.93E−4)	−9.16	0.357 (6.32E−4)	−6.54
$\varepsilon_1=\varepsilon_2=1$, $\tau=2, r_2/r_1=0.5$	0.526	0.545 (0)	3.61	0.5368 (0.0005)	2.05	0.505 (1.54E−4)	−3.99	0.521 (5.79E−4)	−0.95
$\varepsilon_1=\varepsilon_2=1$, $\tau=2, r_2/r_1=0.01$	1	1.2 (0)	20.00	0.955 (0.033)	−4.50	2.35 (0.46528)	135	1.09 (0.050)	9.00
$\varepsilon_1=\varepsilon_2=0.3$, $\tau=2, r_2/r_1=0.1$	0.255	0.27 (0)	5.88	0.2537 (0.0012)	−0.51	0.273 (1.23E−3)	7.06	0.276 (1.28E−3)	8.24
$\varepsilon_1=\varepsilon_2=0.1$, $\tau=2, r_2/r_1=0.1$	0.088	0.094 (0)	6.82	0.0894 (0.0029)	1.59	0.0942 (4.83E−4)	7.05	0.0961 (1.70E−4)	9.20

* RD = Relative discrepancy with respect to Monte Carlo result.

Nondimensional outer wall heat flux $\Psi_1^{*\prime}$s mean values and associated standard deviations are given in Table 2. Due to the use of a local directional coordinate system, standard deviation of the DOM-OCC is zero, while those of the other DOMs are not zero. On the whole, the DOM-FV-RT and DOIM (unstructured) have larger standard deviation values than the DOIM (structured), but they are approximately less than 4% of mean values even for the DOM-FV-RT and DOIM (unstructured).

The relative discrepancies with respect to Monte Carlo results [41] are also tabulated in Table 2 and defined as follows:

$$\text{Relative discrepancy of } \Psi_1^*(\%) = \frac{\Psi_1^*|_{\text{DOM}} - \Psi_1^*|_{\text{Monte Carlo}}}{\Psi_1^*|_{\text{Monte Carlo}}} \times 100 \tag{33}$$

From Table 2, it is shown that the relative discrepancies of the DOM-FV-RT are less than 5% for all the test cases and are the smallest among the three DOMs results. As for the two other methods, the DOM-OCC overestimates Ψ_1^* and the DOIM overestimates or underestimates it depending on the test cases. Their relative discrepancies vary globally between 4 and 16% if the case with the smallest ratio r_2/r_1 is put aside.

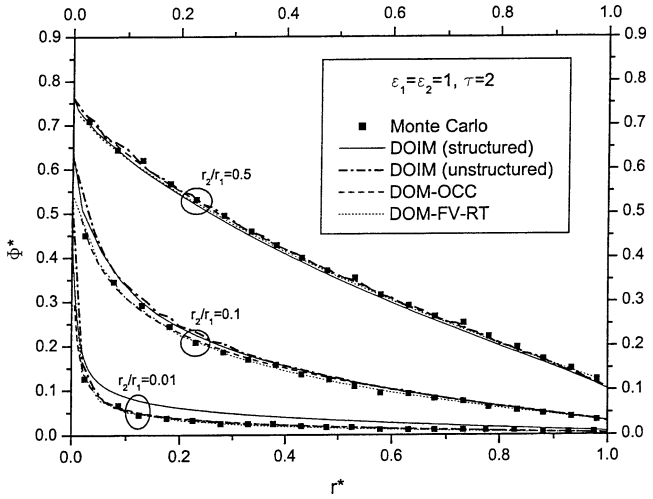

Fig. 6. Nondimensional emissive power distribution of medium for various radius ratios in the circular ring problem.

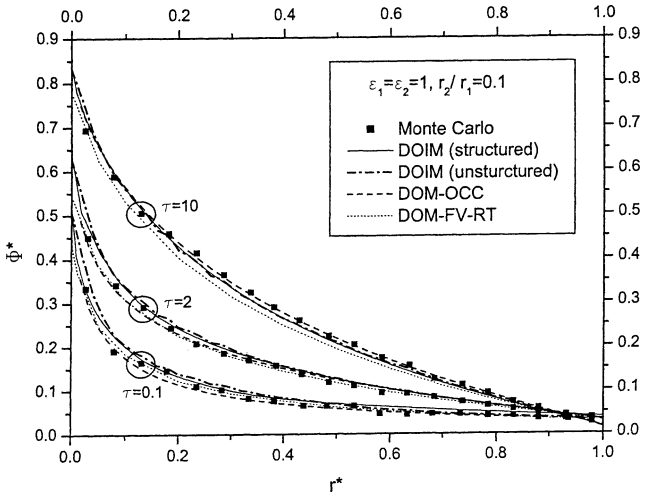

Fig. 7. Nondimensional emissive power distribution of medium for various optical depths in the circular ring problem.

The first cases consider black walled rings with a fixed optical depth ($\tau = 2$) and a radius ratio varying as 0.01, 0.1 and 0.5. The nondimensional emissive powers Φ^* of those media are shown in Fig. 6. The results of the DOM-OCC, DOM-FV-RT and DOIM (unstructured) agree well with Monte Carlo results regardless of radius ratios while a large difference at $r_2/r_1 = 0.01$ appears for the DOIM (structured). Furthermore, for this case, the relative discrepancy of Ψ_1^* is largest for all the three DOMs and the DOIM (structured) and DOM-OCC results cannot be accepted as proper solutions. This is caused by the ray effect. When radius ratio is small, the inner cylinder behaves like a localized heat source. Therefore, enough numbers of spatial grids and angular ordinates need to be taken. However, even for this case, the DOM-FV-RT and to a lesser extent the DOIM (unstructured) show good results. In short, the DOM-FV-RT and DOIM (unstructured) are less sensible to the ray effect and unstructured grid system seems to have advantage over structured one for this kind of problems. With regard to Ψ_1^*, the errors of the DOM-OCC and DOIM (unstructured) decrease as radius ratio increases unlike the other DOMs.

For the second series of tests, the walls are black, the radius ratio r_2/r_1 is fixed at 0.1 and the optical depth is varied as 0.1, 2 and 10. Fig. 7 shows nondimensional emissive power Φ^* of medium for these cases. The figure reveals that all the results obtained by the three DOMs are similar to Monte Carlo ones. However, a slight overestimation for $\tau = 0.1$ and underestimation for $\tau = 10$ can be observed for the DOIM and DOM-FV RT, respectively. As for wall heat fluxes Ψ_1^*, the DOM-FV-RT gives the best results even for $\tau = 10$. Although the DOM-FV-RT underestimates emissive power in the middle of medium for $\tau = 10$, there is little discrepancy near outer wall ($r^* = 1$). Therefore, it can be expected that wall heat flux Ψ_1^* by the DOM-FV-RT for this case is more reasonable than the emissive power. As optical depth increases, the relative discrepancies of Ψ_1^* by the DOM-OCC, DOM-FV-RT and DOIM (unstructured) also increase but that by the DOIM (structured) does not.

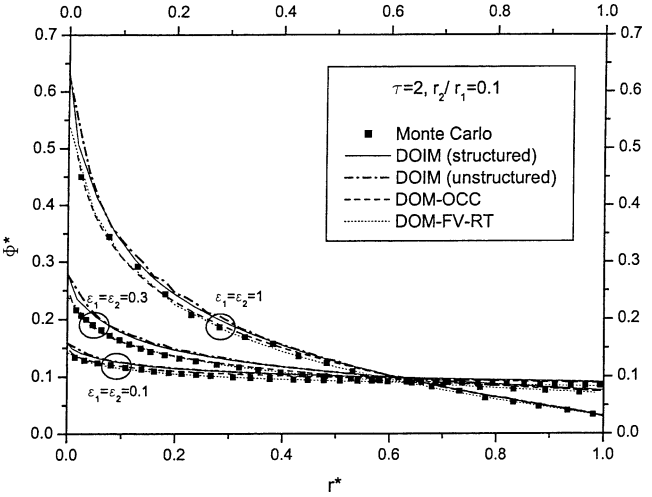

Fig. 8. Nondimensional emissive power distribution of medium for various wall emissivities in the circular ring problem.

The last cases consider a fixed optical depth and radius ratio ($\tau = 2$ and $r_2/r_1 = 0.1$), and a varying wall emissivity (0.1, 0.3 and 1). The case of diffusely reflecting walls will make it possible to evaluate the influence of the accuracy of wall flux calculation on the medium emissive power. The nondimensional emissive power distribution is shown in Fig. 8. The DOM-FV-RT results agree well with Monte Carlo results, the DOM-OCC slightly overestimates, and the DOIM overestimates more than the DOM-OCC. The DOM-FV-RT gives the best wall heat fluxes Ψ_1^* regardless of wall emissivity. It is clear that the error in wall heat fluxes of DOM-OCC and DOIM is reported on emissive power profiles when walls are non-black. However, it should be noticed that the relative discrepancy of Ψ_1^* by the DOM-OCC for black walls is almost twice as large as those for

Table 3
Numbers of spatial grids (or triangular cells) and angular ordinates taken for the entire elliptical ring

Test cases	DOM-OCC*		DOM-FV-RT		DOIM (structured)		DOIM (unstructured)	
	No. of spatial grids	No. of angular ordinates	No. of triangular cells	No. of angular ordinates	No. of spatial grids	No. of angular ordinates	No. of triangular cells	No. of angular ordinates
$\varepsilon_1 = \varepsilon_2 = 1$, $\tau = 10$	19200	64	5100	196	14400	60	7182	240
$\varepsilon_1 = \varepsilon_2 = 1$, $\tau = 1$	16000	48	5100	196	14400	120	7182	240
$\varepsilon_1 = \varepsilon_2 = 1$, $\tau = 0.1$	19200	128	5100	196	7200	120	7182	240
$\varepsilon_1 = \varepsilon_2 = 0.3$, $\tau = 10$	19200	64	5100	196	14400	120	7182	240
$\varepsilon_1 = \varepsilon_2 = 0.3$, $\tau = 1$	19200	48	5100	196	14400	120	7182	240
$\varepsilon_1 = \varepsilon_2 = 0.3$, $\tau = 0.1$	19200	128	5100	196	7200	120	7182	240
$\varepsilon_1 = 1, \varepsilon_2 = 0.1$, $\tau = 10$	19200	64	5100	196	14400	120	7182	240
$\varepsilon_1 = 1, \varepsilon_2 = 0.1$, $\tau = 1$	19200	48	5100	196	14400	120	7182	240
$\varepsilon_1 = 1, \varepsilon_2 = 0.1$, $\tau = 0.1$	19200	128	5100	196	3600	120	7182	240

* For the DOM-OCC, actual number of spatial grids taken in the calculation is a quarter of the value given in this table.

non-black walls, whereas the DOIM gives better results for black walls than for non-black walls.

3.2. Elliptical ring problem

The schematic is shown in Fig. 5(b). The temperatures of the inner and outer walls are 1000 K and 500 K, respectively. The following three wall emissivity cases are considered: $\varepsilon_1 = 1, \varepsilon_2 = 1$; $\varepsilon_1 = 0.3$, $\varepsilon_2 = 0.3$; and $\varepsilon_1 = 1$, $\varepsilon_2 = 0.1$. In each case, the optical thickness τ which is defined as absorption coefficient multiplied by the difference between lengths of semi-major axes, is varied as 0.1, 1 and 10. Again, both enclosures have diffuse and isothermal walls and the medium is assumed to be at radiative equilibrium. In this problem, nondimensional incident heat fluxes at inner and outer walls (Ψ_2^*) are defined as follows:

$$\Psi_2^* = \begin{cases} \dfrac{q''_{\text{incident}}|_{\text{outer wall}}}{\sigma T_1^4} & \text{at outer wall} \\ \dfrac{q''_{\text{incident}}|_{\text{inner wall}}}{\sigma T_2^4} & \text{at inner wall} \end{cases} \tag{34}$$

It is obtained along the dimensionless curvilinear distance along the wall (distance along the wall divided by the perimeter of the ellipse, i.e., $s/s_{\max}$ in Fig. 5(b)). Nondimensional emissive power along major or minor axis (Φ^*) is defined as follows:

$$\Phi^* = \begin{cases} \dfrac{T^4(x, y=0) - T_1^4}{T_2^4 - T_1^4} & \text{along major axis} \\ \dfrac{T^4(x=0, y) - T_1^4}{T_2^4 - T_1^4} & \text{along minor axis} \end{cases} \tag{35}$$

As is done in the circular ring problem, numbers of spatial grids (or triangular cells for the DOIM (unstructured) and DOM-FV-RT) and angular ordinates used for each tested case are mentioned. They are given in Table 3. Unlike the circular ring problem, there is no circumferential symmetry in this problem and a local azimuthal symmetry cannot be further considered. Then the DOM-OCC uses larger numbers of spatial grids and azimuthal angles for this problem than for the circular ring one. With regard to angular domain, the DOIM (unstructured) uses the largest number of angular ordinates and the DOM-FV-RT takes the 2nd largest (T_7 angular quadrature) while the DOM-OCC generally takes the least. Like in the circular ring problem, the DOM-OCC actually handles a quarter of the entire elliptical ring using symmetry, while the DOIM and DOM-FV-RT consider the entire domain for their calculation. Therefore, the DOM-OCC generally needs the least computational efforts. The first cases consider black walls and optical depths τ varying as 0.1, 1 and 10. The nondimensional emissive power distribution Φ^* obtained with these media along major and minor axes are shown in Figs. 9–11. When optical depth τ is 10 or especially 1, results of the three DOMs agree well with each other, and for all the tested cases, emissive power along minor axis is always higher than that along major axis. It is because hot inner wall is less seen along major axis than along minor axis. The nondimensional incident heat fluxes at walls Ψ_2^* are shown in Figs. 12–17 and they present some oscillations in the DOM-FV-RT and DOIM results. It is due to the solid angle overhang at walls for the DOM-FV-RT and DOIM resulting from a

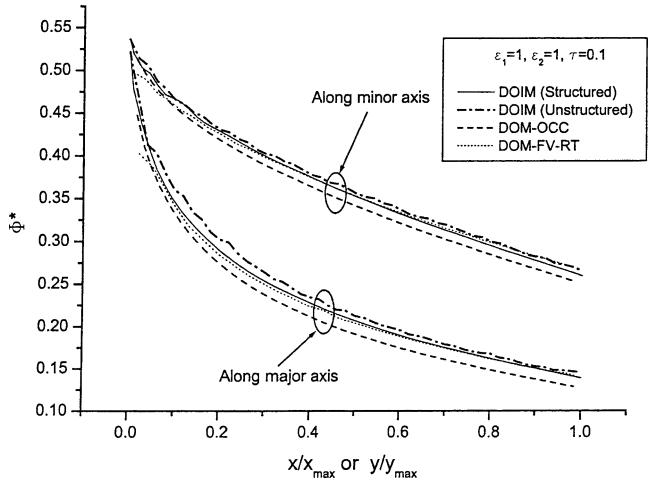

Fig. 9. Nondimensional emissive power distribution of medium for $\varepsilon_1 = \varepsilon_2 = 1$ and $\tau = 0.1$ in the elliptical ring problem.

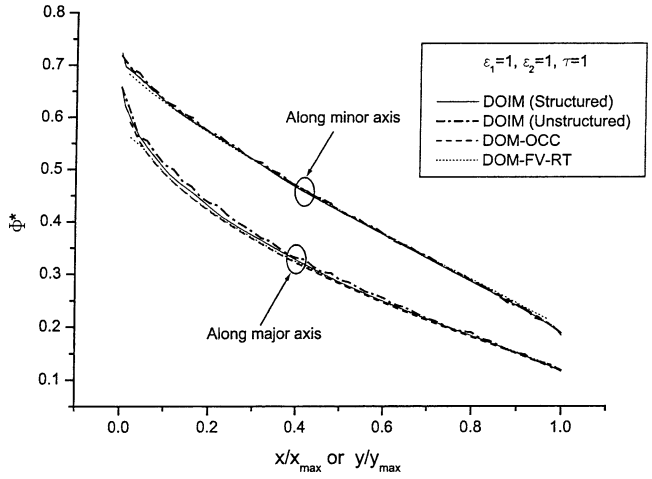

Fig. 10. Nondimensional emissive power distribution of medium for $\varepsilon_1 = \varepsilon_2 = 1$ and $\tau = 1$ in the elliptical ring problem.

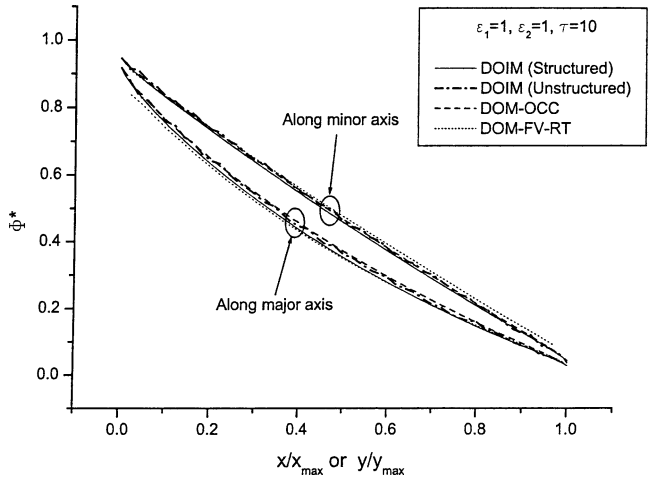

Fig. 11. Nondimensional emissive power distribution of medium for $\varepsilon_1 = \varepsilon_2 = 1$ and $\tau = 10$ in the elliptical ring problem.

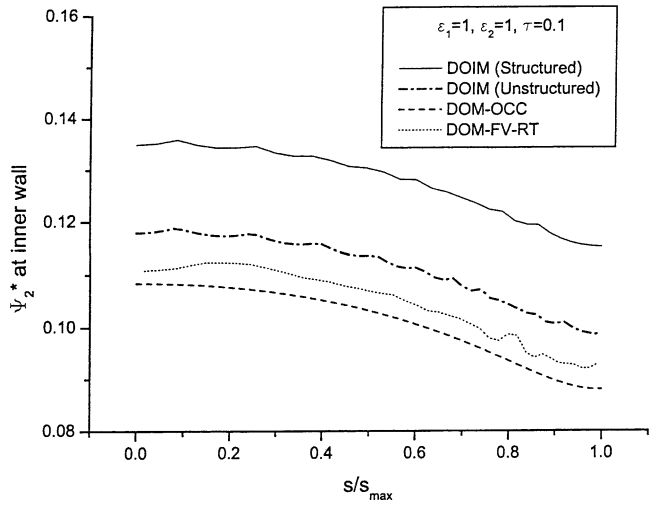

Fig. 12. Nondimensional incident heat flux at inner wall for $\varepsilon_1 = \varepsilon_2 = 1$ and $\tau = 0.1$ in the elliptical ring problem.

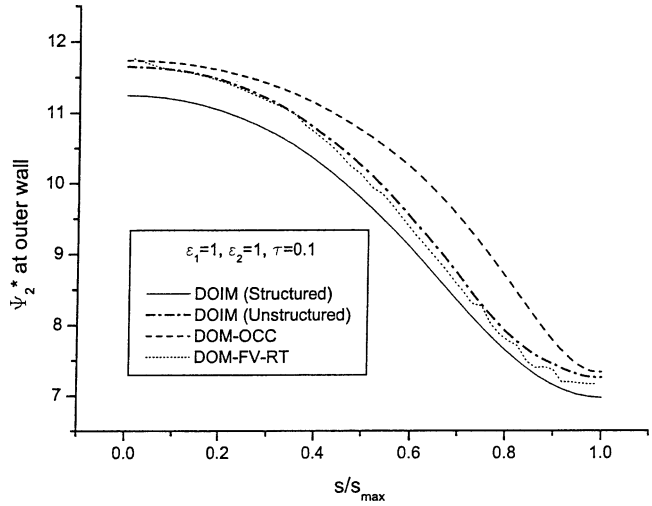

Fig. 13. Nondimensional incident heat flux at outer wall for $\varepsilon_1 = \varepsilon_2 = 1$ and $\tau = 0.1$ in the elliptical ring problem.

fixed angular ordinates set in space, while the DOM-OCC using a local directional coordinate system can avoid the solid angle overhang at walls. Furthermore the DOIM, using PCA quadrature, has less solid angle overhang effect for this elliptical ring problem than the DOM-FV-RT using T_N quadrature. Especially for the DOIM (unstructured), a large number of angular ordinates is used to reduce the solid angle overhang effect at walls. These solid angle overhang effects can be observed in Figs. 12–17.

Generally, the three DOMs give similar results, even if some discrepancies can be observed, specially with the incident heat fluxes. If we take the DOM-OCC that has no oscillation as reference for incident heat fluxes, it is observed from Figs. 12–17 that the DOIM overestimates at inner walls and underestimates at outer walls to keep overall energy balance in respect to the DOM-OCC. The DOM-FV-RT yields results which are similar to those of the DOM-OCC

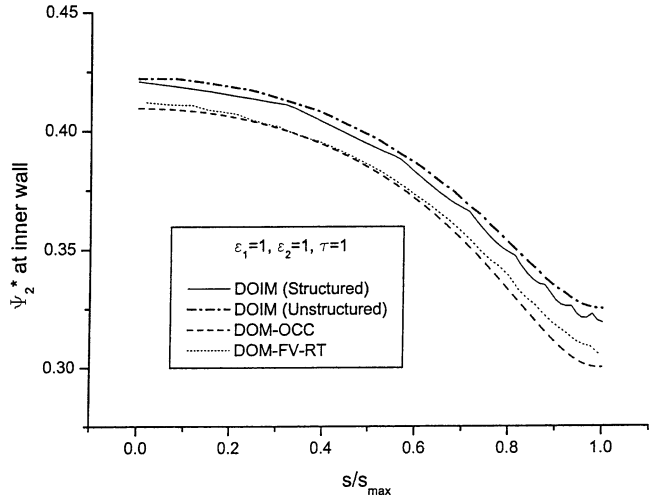

Fig. 14. Nondimensional incident heat flux at inner wall for $\varepsilon_1 = \varepsilon_2 = 1$ and $\tau = 1$ in the elliptical ring problem.

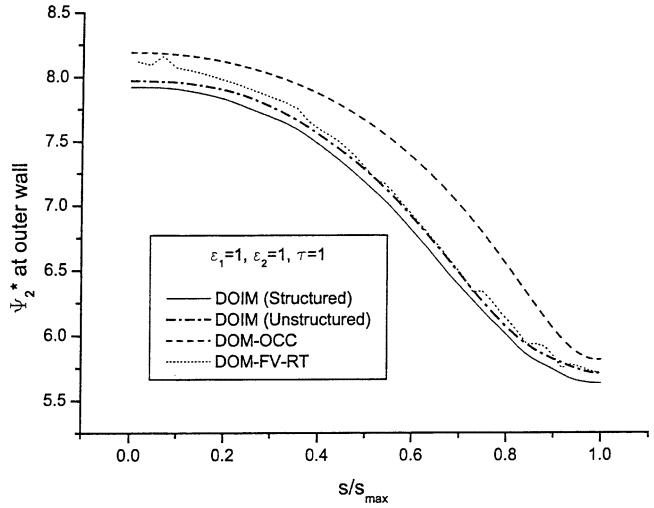

Fig. 15. Nondimensional incident heat flux at outer wall for $\varepsilon_1 = \varepsilon_2 = 1$ and $\tau = 1$ in the elliptical ring problem.

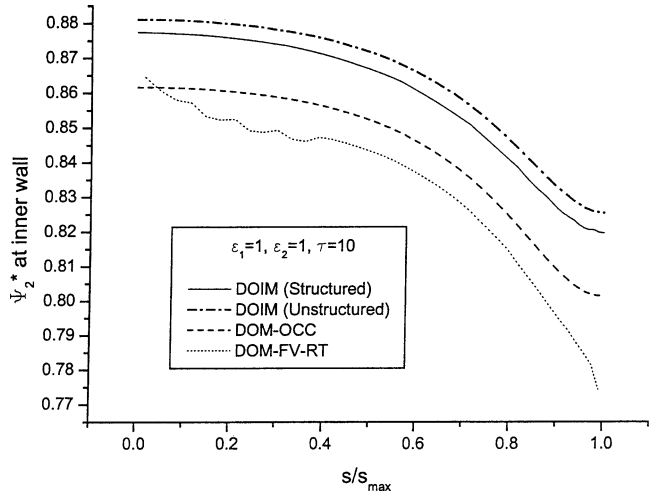

Fig. 16. Nondimensional incident heat flux at inner wall for $\varepsilon_1 = \varepsilon_2 = 1$ and $\tau = 10$ in the elliptical ring problem.

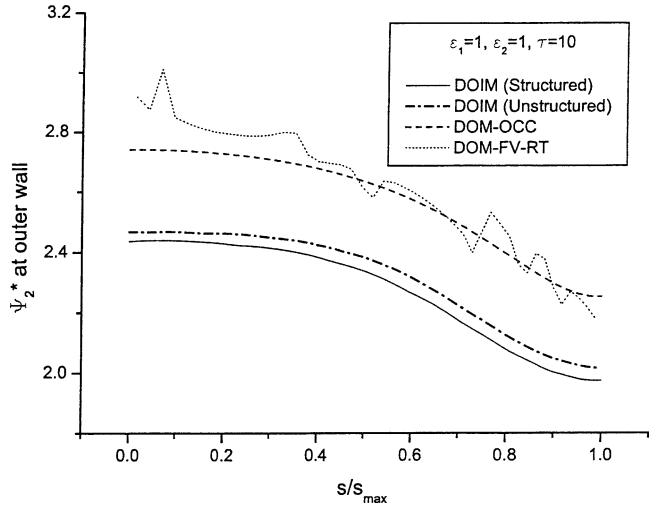

Fig. 17. Nondimensional incident heat flux at outer wall for $\varepsilon_1 = \varepsilon_2 = 1$ and $\tau = 10$ in the elliptical ring problem.

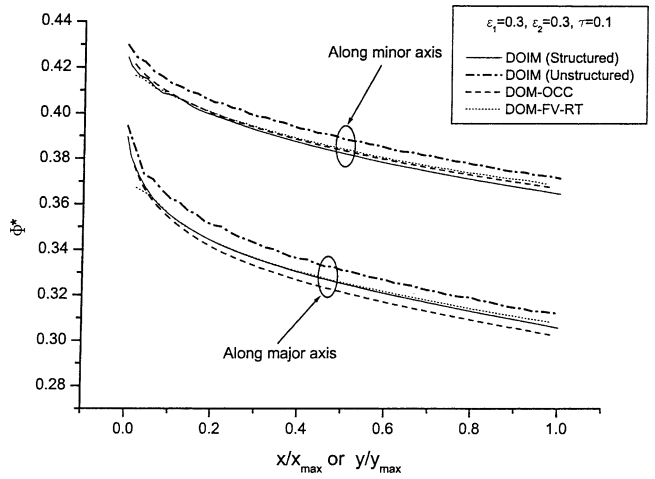

Fig. 18. Nondimensional emissive power distribution of medium for $\varepsilon_1 = \varepsilon_2 = 0.3$ and $\tau = 0.1$ in the elliptical ring problem.

for the inner walls (see Figs. 12, 14 and 16) and somewhat different for the outer walls (see Figs. 13 and 15).

Let us consider $\tau = 1$ case in detail. There is excellent agreement between the three DOMs results for emissive power distribution from Fig. 10. Furthermore, the DOM-OCC and DOM-FV-RT results for incident heat fluxes at inner walls are similar to each other from Fig. 14. However, from Fig. 15, there is a discrepancy between the two results at outer walls. This means that the two methods to adjust overall energy balance by the DOM-OCC and DOM-FV-RT are different from each other in this case, and it seems that this difference may be ascribed to the DOM-FV-RT which has solid angle overhang at walls.

Second, consider the cases that $\varepsilon_1 = \varepsilon_2 = 0.3$ and an optical depth τ is varied as 0.1, 1 and 10. Nondimensional emissive power distributions Φ^* of medium along major and minor axes are shown in Figs. 18–20. The results of the three DOMs generally agree with each other especially for $\tau = 1$

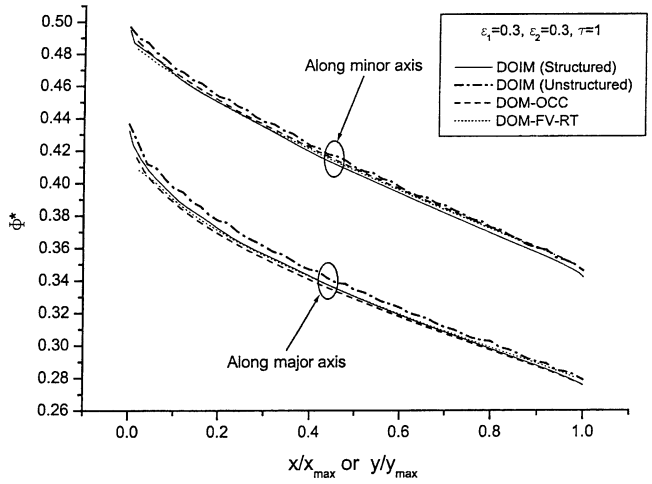

Fig. 19. Nondimensional emissive power distribution of medium for $\varepsilon_1 = \varepsilon_2 = 0.3$ and $\tau = 1$ in the elliptical ring problem.

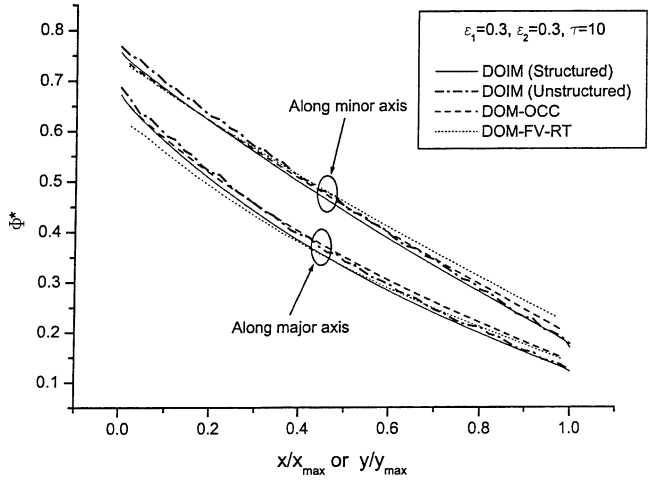

Fig. 20. Nondimensional emissive power distribution of medium for $\varepsilon_1 = \varepsilon_2 = 0.3$ and $\tau = 10$ in the elliptical ring problem.

except that the DOIM (unstructured) gives slightly higher values than the other DOMs. As is for black wall cases, values of Φ^* along minor axis are larger than those along major axis. Furthermore, from the figures, it can be verified that Φ^* values for these reflective wall cases are smaller than those for black wall cases. Nondimensional incident heat fluxes Φ_2^* at walls are given in Figs. 21–26. They do not show as good agreement as emissive power distributions, and some oscillations are observed in the DOM-FV-RT and DOIM (structured) results in these reflective wall cases too. But they are similar within relative error of 10% with regard to the DOM-OCC results.

Lastly, the cases that $\varepsilon_1 = 1$, $\varepsilon_2 = 0.1$ and an optical depth τ is varied as 0.1, 1 and 10 are considered. The nondimensional emissive power distributions along major and minor axes are shown in Figs. 27–29. The best agreement is observed at $\tau = 1$. At $\tau = 0.1$, the DOM-OCC gives slightly lower values than the other methods, while the DOM-FV-RT shows that tendency at $\tau = 10$. In these cases, the values of

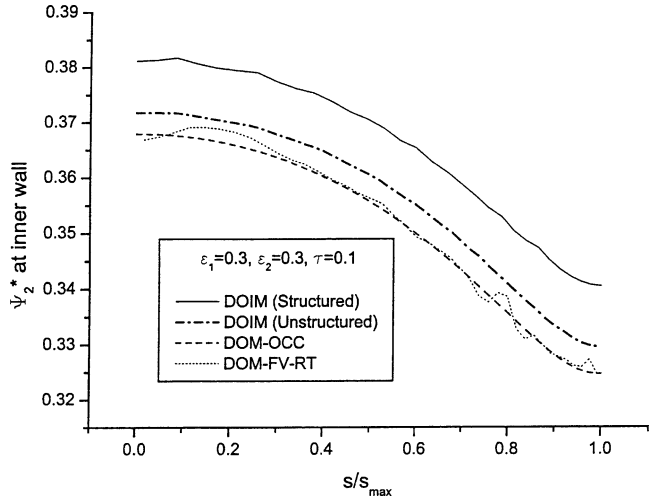

Fig. 21. Nondimensional incident heat flux at inner wall for $\varepsilon_1 = \varepsilon_2 = 0.3$ and $\tau = 0.1$ in the elliptical ring problem.

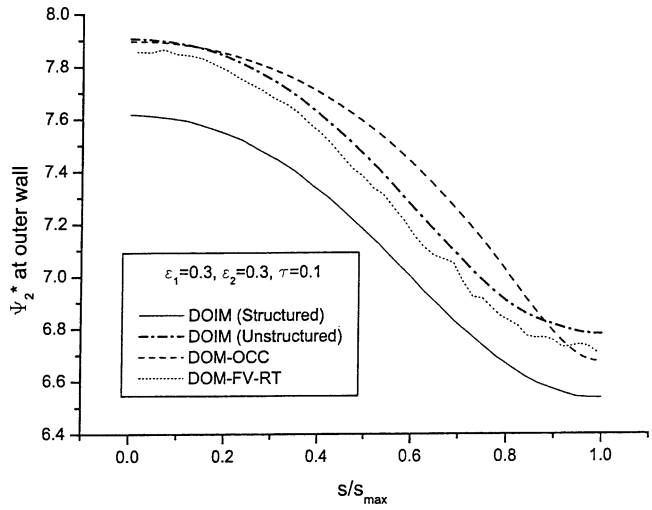

Fig. 22. Nondimensional incident heat flux at outer wall for $\varepsilon_1 = \varepsilon_2 = 0.3$ and $\tau = 0.1$ in the elliptical ring problem.

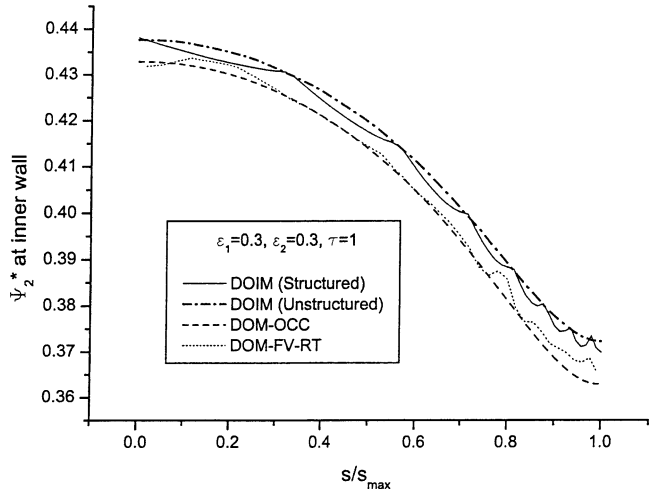

Fig. 23. Nondimensional incident heat flux at inner wall for $\varepsilon_1 = \varepsilon_2 = 0.3$ and $\tau = 1$ in the elliptical ring problem.

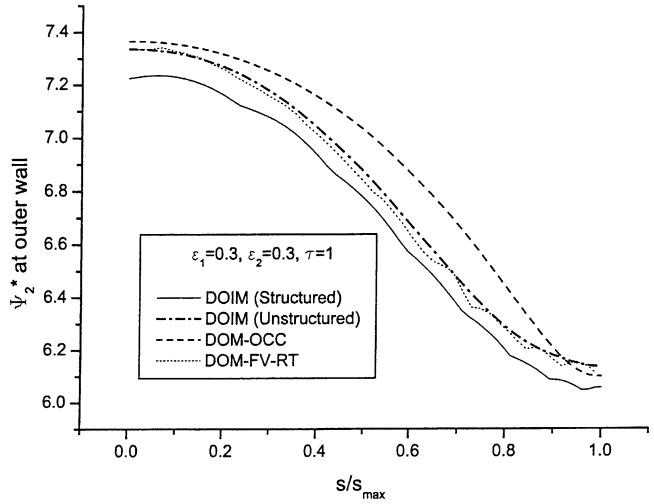

Fig. 24. Nondimensional incident heat flux at outer wall for $\varepsilon_1 = \varepsilon_2 = 0.3$ and $\tau = 1$ in the elliptical ring problem.

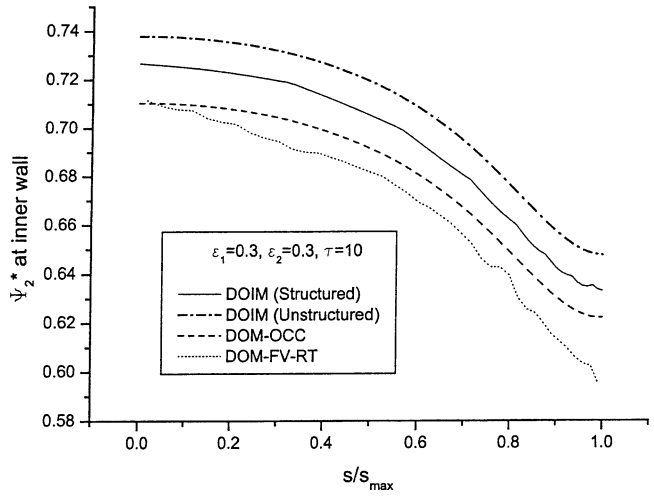

Fig. 25. Nondimensional incident heat flux at inner wall for $\varepsilon_1 = \varepsilon_2 = 0.3$ and $\tau = 10$ in the elliptical ring problem.

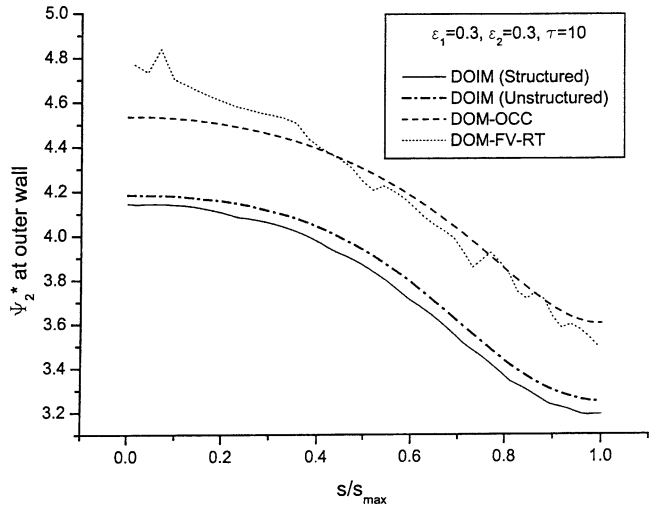

Fig. 26. Nondimensional incident heat flux at outer wall for $\varepsilon_1 = \varepsilon_2 = 0.3$ and $\tau = 10$ in the elliptical ring problem.

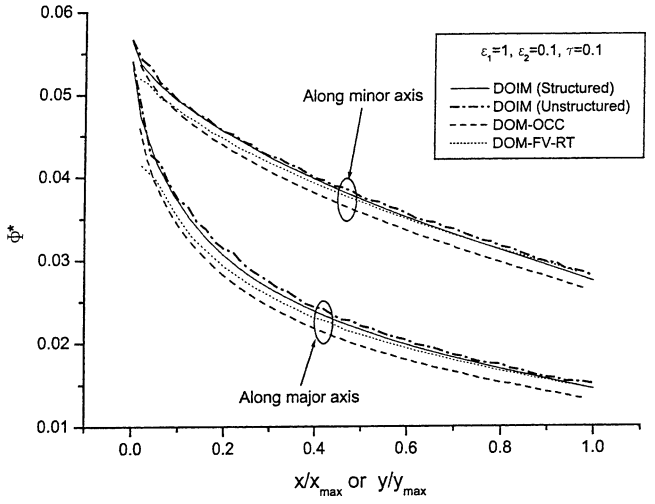

Fig. 27. Nondimensional emissive power distribution of medium for $\varepsilon_1 = 1$, $\varepsilon_2 = 0.1$ and $\tau = 0.1$ in the elliptical ring problem.

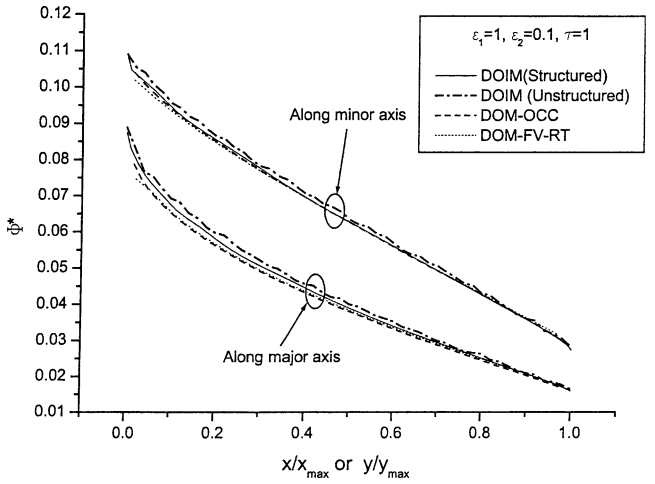

Fig. 28. Nondimensional emissive power distribution of medium for $\varepsilon_1 = 1$, $\varepsilon_2 = 0.1$ and $\tau = 1$ in the elliptical ring problem.

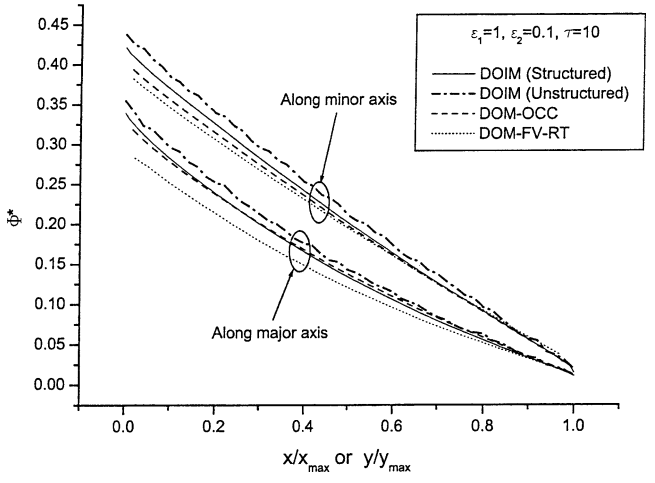

Fig. 29. Nondimensional emissive power distribution of medium for $\varepsilon_1 = 1$, $\varepsilon_2 = 0.1$ and $\tau = 10$ in the elliptical ring problem.

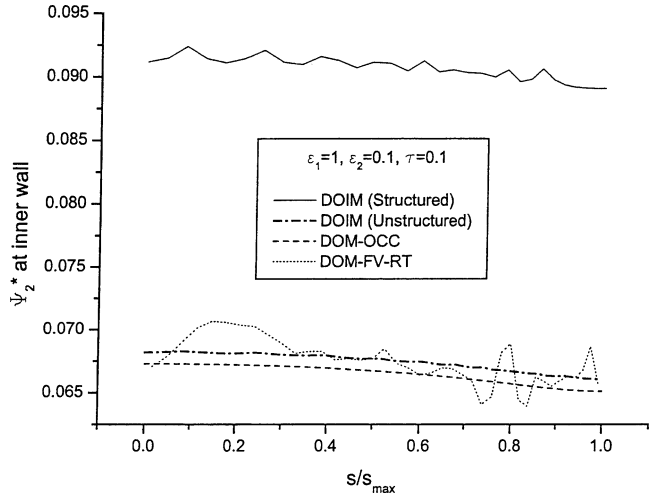

Fig. 30. Nondimensional incident heat flux at inner wall for $\varepsilon_1 = 1, \varepsilon_2 = 0.1$ and $\tau = 0.1$ in the elliptical ring problem.

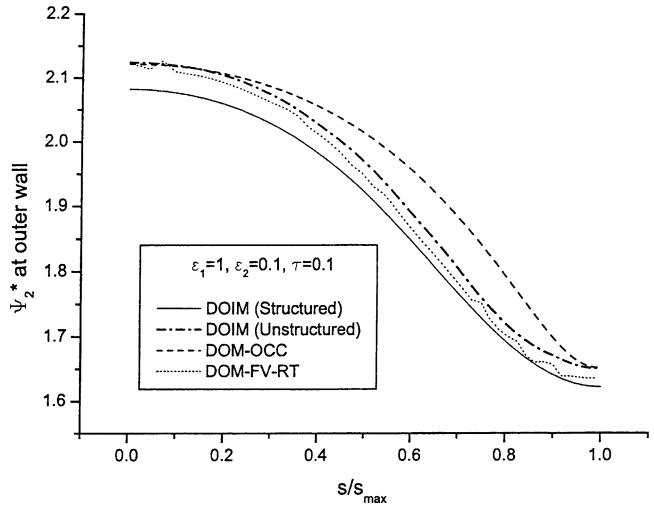

Fig. 31. Nondimensional incident heat flux at outer wall for $\varepsilon_1 = 1, \varepsilon_2 = 0.1$ and $\tau = 0.1$ in the elliptical ring problem.

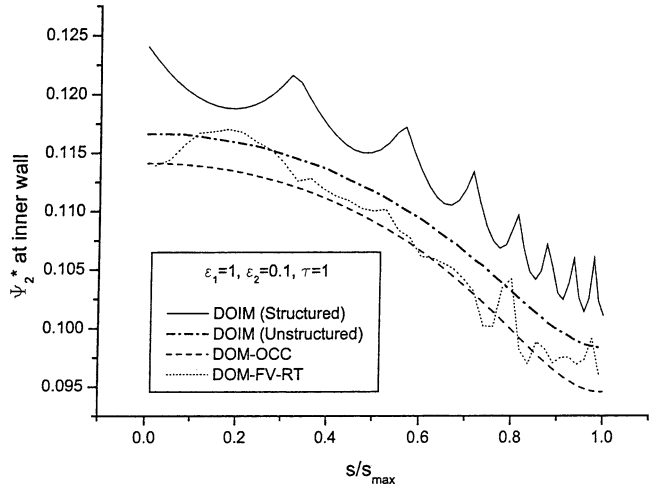

Fig. 32. Nondimensional incident heat flux at inner wall for $\varepsilon_1 = 1, \varepsilon_2 = 0.1$ and $\tau = 1$ in the elliptical ring problem.

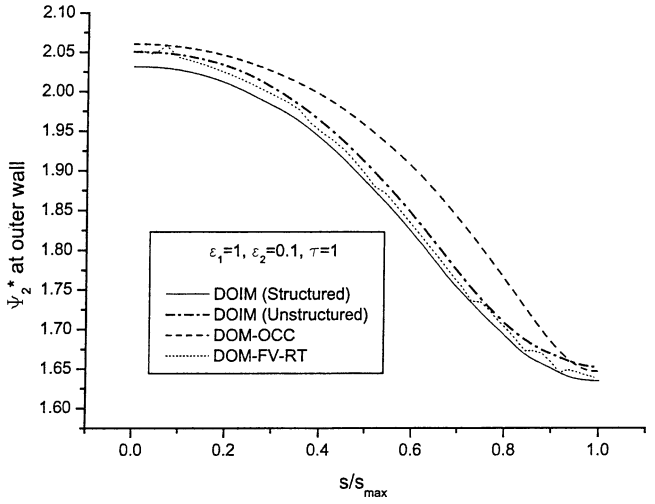

Fig. 33. Nondimensional incident heat flux at outer wall for $\varepsilon_1 = 1, \varepsilon_2 = 0.1$ and $\tau = 1$ in the elliptical ring problem.

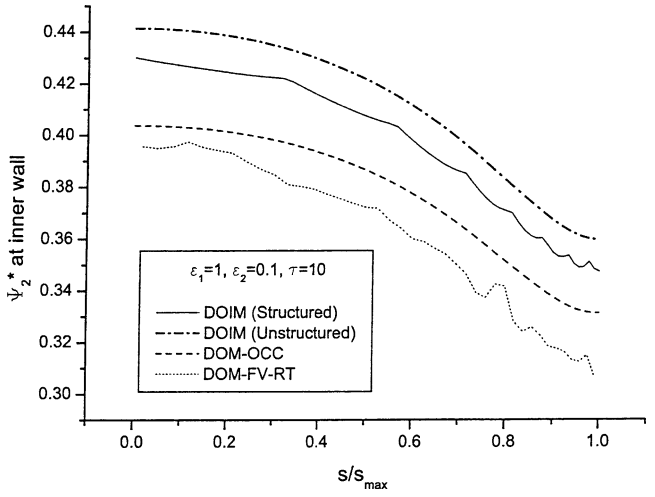

Fig. 34. Nondimensional incident heat flux at inner wall for $\varepsilon_1 = 1, \varepsilon_2 = 0.1$ and $\tau = 10$ in the elliptical ring problem.

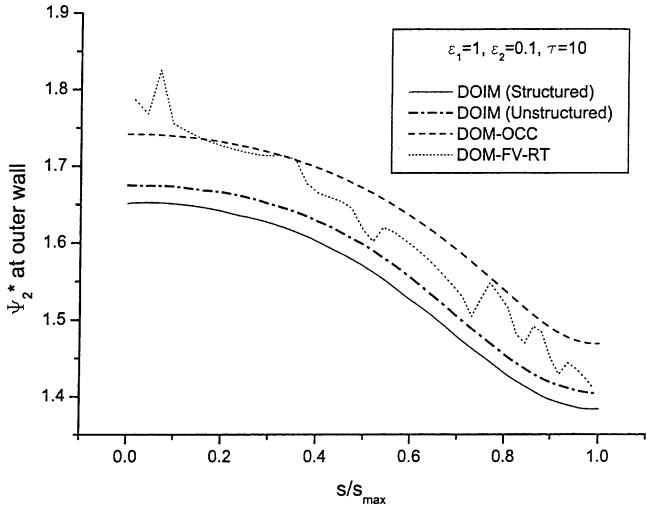

Fig. 35. Nondimensional incident heat flux at outer wall for $\varepsilon_1 = 1, \varepsilon_2 = 0.1$ and $\tau = 10$ in the elliptical ring problem.

Φ^* along minor axis are larger than those along major axis. The inner wall is highly reflective in these cases and considerable decrease in Φ^* is observed from the figures compared to black wall cases. Nondimensional incident heat fluxes Ψ_2^* at walls are shown in Figs. 30–35. Oscillations are observed in the DOM-FV-RT and DOIM (structured) results and they are severe at highly reflective inner wall. As is for all other tested cases, incident heat fluxes at walls do not give as good agreement as emissive power distributions. However, they are similar within relative error of 10% with regard to the DOM-OCC results except at inner wall with $\tau = 0.1$.

4. Conclusion

Three variations of the DOM have been applied to the two-dimensional curved geometries. Results have been carefully analysed to yield specific performances associated to all methods or to some of them:

- the three methods give quite similar and acceptable results in terms of medium temperature (emissive power distribution),
- it has been shown that for a localised heat source (the circular cylinder test case with the smallest radius ratio), the DOM-OCC and the DOIM (structured) are sensible to the ray effect whereas the DOIM (unstructured) and the DOM-FV-RT are much less. The use of unstructured grids seems to have advantage over the use of structured ones for this kind of situation,
- the DOM-OCC is able, even for a curved geometry, to take advantage of spatial symmetries to reduce spatial and directional calculation domains. However, it is restricted to geometries which can be described in orthogonal curvilinear coordinates whereas the DOIM and the DOM-FV-RT can be applied to any kind of 2D complex enclosure,
- for radiation fluxes at walls, the performances of the three DOMs are not identical both for the circular and elliptical rings test cases. Since the DOM-FV-RT and the DOIM use Cartesian coordinates and angular ordinates fixed in space, there exist solid angle overhangs at walls when the boundaries are not parallel to a plane of coordinates. Therefore, they produce oscillations in wall radiation fluxes along boundaries, whereas the DOM-OCC does not, thanks to the use of a local directional coordinates system. In terms of absolute accuracy, the DOM-FV-RT gives the best results compared to the other ones for the circular cylinder test cases. The performances of the DOIM and the DOM-OCC depend on the case under consideration. For the elliptical ring test, the three methods do not adjust overall energy balance in the same way and then lead to different wall radiation flux values within 10% of relative error with regard to DOM-OCC (taken here as a reference because it avoids oscillations). The oscillations produced by the DOM-FV-RT and the DOIM are particularly severe when the walls are highly reflecting.

It is expected that these conclusions should help in improving the DOM, one of the most promising Radiative Transfer Equation solvers when they are applied to complex curved geometries. In particular, a proper attention should be paid to increase the accuracy of the methods for evaluation of wall radiation fluxes, in term of absolute values and of regular variations along the boundaries (avoidance of oscillations) when the walls are not parallel to a plane of coordinates. As further work, tests might be extended to more complex geometries (for the DOIM and the DOM-FV-RT; the DOM-OCC should be first extended to generalised curvilinear coordinates) and to the case of specular reflecting curved boundaries.

References

[1] S. Chandrasekhar, Radiative Transfer, Dover, New York, 1960.
[2] A. Borges De Miranda, J.F. Sacadura, An alternative formulation of the Sn discrete ordinates for predicting radiative transfer in nongray gases, ASME J. Heat Transfer 118 (3) (1996) 650–653.
[3] W.A. Fiveland, J.P. Jessee, Finite element formulation of the discrete ordinates method for multidimensional geometries, J. Thermophys. Heat Transfer 8 (3) (1994) 426–433.
[4] K.B. Cheong, T.H. Song, Examination of solution methods for the second-order discrete ordinate formulation, Numer. Heat Transfer B 27 (1995) 155–173.
[5] R. Koch, W. Krebs, S. Wittig, R. Viskanta, A parabolic formulation of the discrete ordinates method for the treatment of complex geometries, in: M.P. Mengüç (Ed.), Proceedings of the International Symposium on Radiative Heat Transfer, Begell House, 1996, pp. 43–61.
[6] H.-M. Koo, K.-B. Cheong, T.-H. Song, Schemes and applications of first and second order discrete interpolation methods to irregular two-dimensional geometries, ASME J. Heat Transfer 119 (1997) 730–737.
[7] J. Liu, H.M. Shang, Y.S. Chen, Analysis of discrete ordinates method with even parity formulation, J. Thermophys. Heat Transfer 11 (2) (1997) 253–260.
[8] B.G. Carlson, Solution of the transport equation by Sn approximations, Los Alamos Scientific Laboratory Report, LA-1599, 1953.
[9] W.A. Fiveland, Discrete ordinates solutions of the radiation transport equation for rectangular enclosures, ASME J. Heat Transfer 106 (1984) 699–706.
[10] A. Jamalludin, P.J. Smith, Predicting radiative heat transfer in rectangular enclosures using the discrete ordinates method, Comb. Sci. Tech. 59 (1988) 321–340.
[11] J.S. Truelove, Three dimensional radiation in absorbing-emitting-scattering media using the discrete ordinates approximation, J. Quant. Spectrosc. Radiat. Transfer 42 (3) (1989) 187–189.
[12] W.A. Fiveland, A discrete ordinates method for predicting radiative heat transfer in axisymmetric enclosures, ASME Paper, 82-HT-20, 1982.
[13] A. Yücel, L. Williams, Azimuthally dependent radiative transfer in cylindrical geometry, Fund. Appl. Heat Transfer ASME HTD 72 (1987) 29–37.
[14] A. Jamalludin, P.J. Smith, Predicting radiative heat transfer in axisymmetric cylindrical enclosures using the discrete ordinates method, Comb. Sci. Tech. 62 (1988) 173–186.
[15] J.R. Tsai, M.N. Özisik, Radiation in cylindrical symmetry with anisotropic scattering and variable properties, Internat. J. Heat Mass Transfer 33 (12) (1990) 2651–2658.

[16] S. Jendoubi, H.S. Lee, T.-K. Kim, Discrete ordinates solutions for radiatively participating media in a cylindrical enclosure, J. Thermophys. Heat Transfer 7 (2) (1993) 213–219.
[17] J.R. Tsai, M.N. Özisik, F. Santarelli, Radiation in spherical symmetry with anisotropic scattering and variable properties, J. Quant. Spectrosc. Radiat. Transfer 39 (1) (1988) 27–31.
[18] R. Vaillon, M. Lallemand, D. Lemonnier, Radiative heat transfer in orthogonal curvilinear coordinates using the discrete ordinates method, J. Quant. Spectrosc. Radiat. Transfer 55 (1) (1996) 7–17.
[19] R. Vaillon, M. Lallemand, D. Lemonnier, Radiative equilibrium in axisymmetric semi-transparent gray shells using the discrete ordinates method, in: M.P. Mengüç (Ed.), Proceedings of the International Symposium on Radiative Heat Transfer, Begell House, 1996, pp. 62–74.
[20] E.H. Chui, G.D. Raithby, Computation of radiant heat transfer on a nonorthogonal mesh using the finite-volume method, Numer. Heat Transfer B 23 (1993) 269–288.
[21] J.C. Chai, H.S. Lee, S.V. Patankar, Finite volume method for radiation heat transfer, J. Thermophys. Heat Transfer 8 (3) (1994) 419–425.
[22] V. Le Dez, A. Charette, Application of the discrete ordinates method to a bidimensional grey medium of complex shape in radiative equilibrium, in: D. Lemonnier, J.B. Saulnier, M. Fiebig (Eds.), Proceedings of the Eurotherm Seminar 36, Elsevier, Amsterdam, 1996, pp. 331–338.
[23] M. Sakami, A. Charette, V. Le Dez, Application of the discrete ordinates method to combined conductive and radiative heat transfer in a two-dimensional complex geometry, J. Quant. Spectrosc. Radiat. Transfer 56 (4) (1996) 517–533.
[24] B.G. Carlson, K.D. Lathrop, Transport Theory. The Method of Discrete Ordinates, Computing Methods in Reactor Physics, Gordon and Breach, 1968.
[25] K.D. Lathrop, Spatial differencing of the transport equation. Positivity vs. accuracy, J. Comput. Phys. 4 (1969) 475–498.
[26] C.P. Thurgood, A critical evaluation of the discrete ordinates method using heart and TN quadrature, Ph.D. Thesis, Department of Chemical Engineering, Quenn's University, Kingston, 1992.
[27] J.P. Jessee, W.A. Fiveland, Bounded, high resolution differencing schemes applied to the discrete ordinates method, J. Thermophys. Heat Transfer 11 (4) (1997) 540–548.
[28] J.P. Jenal, P.J. Erickson, W.A. Rhoades, D.B. Simpson, M.L. Williams, The generation of a computer library for discrete ordinates quadrature sets, Oak Ridge National Laboratory, TM-6023, 1977.
[29] W.A. Fiveland, The selection of discrete ordinate quadrature sets for anisotropic scattering, Fund. Radiat. Heat Transfer ASME HTD 160 (1991) 89–96.
[30] N. El Wakil, J.F. Sacadura, Some improvements of the discrete ordinates method for the solution of the radiative transport equation in multidimensional anisotropically scattering media, Dev. Radiat Heat Transfer ASME HTD 203 (1992) 119–128.
[31] R. Koch, W. Krebs, S. Wittig, R. Viskanta, Discrete ordinates quadrature schemes for multidimensional radiative transfer, J. Quant. Spectrosc. Radiat. Transfer 53 (4) (1995) 353–372.
[32] N. Selçuk, N. Kayakol, Evaluation of discrete ordinates method for radiative heat transfer in rectangular furnaces, Internat. J. Heat Mass Transfer 40 (2) (1997) 213–222.
[33] J.F. Carew, G. Zamonsky, Uniform positive-weight quadratures for discrete ordinate transport calculations, Nucl. Sci. Engrg. 131 (1999) 199–207.
[34] M. Sakami, A. Charette, V. Le Dez, Radiative heat transfer in three-dimensional enclosures of complex geometry by using the discrete ordinates method, J. Quant. Spectrosc. Radiat. Transfer 59 (1/2) (1998) 117–136.
[35] M. Song, R. Viskanta, Discrete ordinates solution of axisymmetric radiative transfer within a condensed semitransparent medium having specularly reflecting boundaries, ASME HTD 325 (3) (1996) 55–62.
[36] W.A. Fiveland, Discrete ordinates method for predicting radiative heat transfer in isotropically and anisotropically scattering media, ASME J. Heat Transfer 109 (1987) 809–812.
[37] J.C. Chai, H.S. Lee, S.V. Patankar, Improved treatment of scattering using the discrete ordinates method, ASME J. Heat Transfer 116 (1994) 260–263.
[38] T.-K. Kim, H. Lee, Effect of anisotropic scattering on radiative heat transfer in two-dimensional rectangular enclosures, Internat. J. Heat Mass Transfer 31 (8) 1711–1721.
[39] K.B. Cheong, T.H. Song, An alternative discrete ordinates method with interpolation and source differencing for two-dimensional radiative transfer problems, Numer. Heat Transfer B 32 (1997) 107–125.
[40] H. Cha, J.W. Yoo, T.H. Song, Discrete ordinates interpolation method for solution of radiative transfer equation in arbitrary 2-D geometry and unstructured grid system, in: Proceedings of the 11th Internat. Heat Transfer Conference, Vol. 7, Taylor & Francis, Washington, DC, 1998, pp. 267–274.
[41] M. Perlmutter, J.R. Howell, Radiant transfer through a gray gas between concentric cylinders using Monte Carlo, ASME J. Heat Transfer C 86 (1964) 169–179.
[42] J.S. Truelove, Discrete ordinate solutions of the radiation transport equation, ASME J. Heat Transfer 109 (1987) 1048–1051.
[43] L.L. Briggs, W.F. Miller, E.E. Lewis, Ray-effect mitigation in discrete ordinate-like angular finite element approximations in neutron transport, Nucl. Sci. Tech. 57 (1975) 205–217.
[44] J.Y. Murthy, S.R. Mathur, Finite volume method for radiative heat transfer using unstructured meshes, J. Thermophys. Heat Transfer 12 (3) (1998) 313–321.